

ORIGINAL RESEARCH ARTICLE

Flexural behavior of 3D printed bio-inspired interlocking suture structures

Sachini Wickramasinghe¹, Truong Do², Phuong Tran^{1*}

¹Department of Civil and Infrastructure Engineering, RMIT University, Melbourne, Australia

²College of Engineering and Computer Science, VinUniversity, Hanoi, Vietnam

Abstract

Additive manufacturing has allowed producing various complex structures inspired by natural materials. In this research, the bio-inspired suture structure was 3D printed using the fused deposition modeling printing technique to study its bending response behavior. Suture is one of the most commonly found structures in biological bodies. The primary purpose of this structure in nature is to improve flexibility by absorbing energy without causing permeant damage to the biological structure. An interesting discovery of the suture joint in diabolical ironclad beetle has given a great opportunity to further study the behavior of these natural suture designs. Inspired by the elliptical shape and the interlocking features of this suture, specimens were designed and 3D printed using polylactic acid thermoplastic polymer. A three-point bending test was then conducted to analyze the flexural behavior of each suture design, while digital image correlation and numerical simulation were performed to capture the insights of deformation process.

Keywords: Suture structure; Fused deposition modeling; Three-point bending; Digital image correlation; Numerical simulation

*Corresponding author:
Phuong Tran
(jonathan.tran@rmit.edu.au)

Citation: Wickramasinghe S, Do T, Tran P, 2022, Flexural behavior of 3D printed bio-inspired interlocking suture structures. *Mater Sci Addi Manuf.* 1(2): 9.
<https://doi.org/10.18063/msam.v1i2.9>

Received: March 17, 2022

Accepted: April 12, 2022

Published Online: May 26, 2022

Copyright: © 2022 Author(s). This is an Open Access article distributed under the terms of the Creative Commons Attribution License, permitting distribution, and reproduction in any medium, provided the original work is properly cited.

Publisher's Note: Whioce Publishing remains neutral with regard to jurisdictional claims in published maps and institutional affiliations.

1. Introduction

Throughout the years of evolution, nature has developed and optimized complex structures to achieve specific functions in every biological body. These complex structures inspire the development of materials and structures with enhanced performances^[1,2]. Three-dimensional (3D) printing or additive manufacturing (AM) has made it possible to recreate these complex natural structures and adapt them into engineering applications to improve their functionalities^[3-7].

Among various natural structures, suture interfaces are visible in a wide range of species and have independently evolved to optimize the performance of diverse biological systems. Suture structures can be found in mammal crania, deer skull, turtle carapace, red-bellied woodpecker beak, boxfish armor, diatoms, and insect cuticles^[8-14]. They provide flexibility to the structure to allow large deformations to absorb impact energy and damp shocks while maintaining structural integrity^[15-17]. Depending on the species, the complexity, interlocking features, and sutures' geometry vary to achieve targeted properties^[18,19]. For example, triangular sutures can be found in woodpecker beak and interlocking complex suture designs can be found in ammonite shells and diatoms, while elliptical shape interlocking sutures are visible in diabolical ironclad beetle^[20]

The recent discovery of the suture structure in diabolical ironclad beetle (*Phloeodes diabolicus*) has attracted many researchers to study its behavior under different test conditions^[24]. This beetle species acts dead to protect from predators since they are unable to fly. The flying beetles have hardened forewings, which act as a protection layer for underlying hindwings^[25-28]. The elytra of the diabolical ironclad beetle perform remarkable crush resistance from predators in nature. The tough exoskeleton is a result of fusion of two elytra by a suture joint, which runs along the whole length of the abdomen. These interlocking sutures with ellipsoidal geometry, known as blades, are tougher than the triangular and hemispherical blades, which are commonly found in other terrestrial beetles. Figure 1D-F shows the diabolical ironclad beetle, a cross-section of the elytra and the suture connection between two elytra. The suture joints in diabolical ironclad beetle help to resist bending moments to protect vital internal organs. By incorporating interlocking suture interfaces into a biological system, the energy dissipation of the structure is regulated^[24,29-31].

Most biological structures contain complex hierarchical arrangements that are difficult to fabricate through conventional manufacturing techniques^[32,33]. Due to the design freedom, quality of the product and process control ability, 3D printing has the potential to develop lightweight complex structures^[34-36]. Among various AM techniques, fused deposition modeling (FDM) – a trademark of Stratasys or fused filament fabrication – a commonly used term by open hardware community/RepRap is a convenient printing method for developing bio-inspired

structures and understanding the mechanical responses and their governing mechanisms^[37-39]. FDM printing is a material extrusion technique where thermoplastic material is melted and extruded through a hot end to create the printing layers^[40]. Performing mechanical testing on 3D printed bio-inspired structures is beneficial in developing guidelines for future modifications and optimizations of the designs. While AM materials have different properties than natural materials, continuous structural design optimizations and mechanical testing would help to understand the failures, deformations, and damages in biological structures^[41,42].

In this research work, diabolical ironclad beetle's suture-inspired designs were printed using polylactic acid (PLA), one of the most popular thermoplastic materials used in FDM printing due to their biodegradability and ease of printing, good strength, and stiffness^[43-46]. The flexural behavior was then analyzed using a three-point bending test, followed by digital image correlation (DIC) and numerical simulation to provide more insight into the bending response of the suture structure. As mentioned before, since the suture joint helps resist bending moments in the beetle structure to protect internal organs, the research is focused on understanding the flexural properties of this bio-inspired suture structure. This suture interlocking mechanism would be greatly beneficial in connecting dissimilar materials without any external joining techniques and connecting small parts could develop large modular parts through interlocking without limiting to the small print volume in many 3D printers.

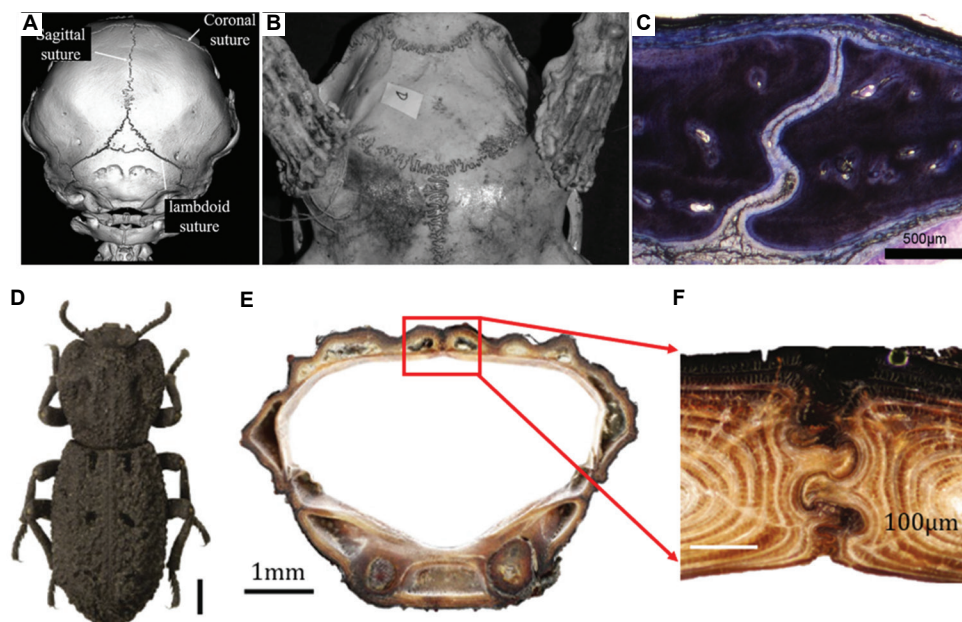


Figure 1. (A) Skull of a domestic shorthair cat^[21], (B) cranial suture in white-tailed deer^[22], (C) alligator internal nasal suture^[23], (D) *Phloeodes diabolicus*, (E) cross-section of the elytra, (F) suture that connects two elytra (with copyright permission from the journal)^[24]

2. Materials and methodology

2.1. Specimen fabrication

The shape of the suture is designed to be elliptical where the ratio between “a” (minor radius) and “b” (major radius) is 1:1.8, while the angle (Θ) between two ellipses is maintained to be 25° as shown in Figure 2A. Design parameters were selected from the literature, where researchers have analyzed the dimensions of the diabolical ironclad beetle’s suture structure^[24]. All the specimens were fabricated using a FDM technique with $45^\circ/-45^\circ$ print orientation. In comparison to $0^\circ/90^\circ$ print orientation, $45^\circ/-45^\circ$ print orientation contains less porous areas in the printed structure as per the X-ray micro-CT scan images in Figure 2B and D. The curved edges in the sutures are perfectly covered in each layer by $45^\circ/-45^\circ$ print orientation. Still, in $0^\circ/90^\circ$ print orientation, the 90° layers could not completely cover the curved edges of the printed structure as shown in microscopic images in Figure 2C and E. PLA specimens are printed using the Prusa Mk3i printer. The suture pattern is inspired by the interlocking connection between the two elytra in the diabolical ironclad beetle (*P. diabolicus*).

Three different sizes of sutures were printed using PLA as S1, S2, and S3; schematic diagrams are given in Figure 3A-C.

Specimens were configured by connecting the two separate parts, printed together without any additional

force. Due to the high dimensional accuracy in the printer, two pieces were printed with the exact dimensions without including gap tolerance. Finally, the pieces were easily fitted together like a jigsaw puzzle without affecting the strength of the final part. The S3 design was further subjected to testing to analyze the effect of the positioning angle of the suture interface since, in nature, suture structure does not always follow a precise straight path, as shown in Figure 1A-D. Nearly straight suture lines are visible in infant skull, but in many cases, sutures create complex arrangement^[47-49]. The schematic and PLA specimens with slanted suture interface by 2° , 5° , and 8° are given in Figure 3D-F, respectively. Dimensions of S1, S2, and S3 specimens are given in Table 1. Dimensions of S3- 2° , S3- 5° , and S3- 8° are also similar to the dimensions of S3. The areas covered by the suture interfaces in all three sizes are maintained to be $\sim 3.65 \text{ cm}^2$, which are calculated by the complete elliptic integral of the second kind, multiplied by the thickness of the specimen.

$$c = 4 \int_0^{\frac{\pi}{2}} \sqrt{a^2 \cos^2 \theta + b^2 \sin^2 \theta} d\theta, \quad (\text{Eq. 1})$$

$$c' = \int_0^t \sqrt{a^2 \cos^2 \theta + b^2 \sin^2 \theta} d\theta, \quad (\text{Eq. 2})$$

$$a \tan\left(\frac{b}{a} \tan \theta\right) = t \quad (\text{Eq. 3})$$

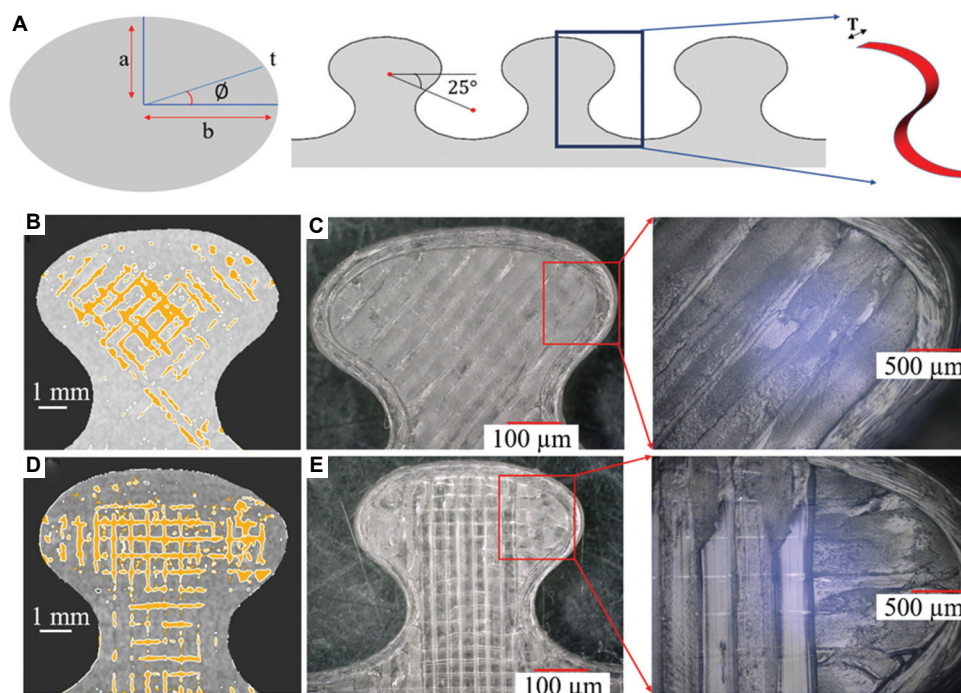


Figure 2. (A) Schematic of the suture design, (B) X-ray micro-CT scan of $45^\circ/-45^\circ$ print orientation, (C) microscopic images of $45^\circ/-45^\circ$ print orientation, (D) X-ray micro-CT scan of $0^\circ/90^\circ$ print orientation, (E) microscopic images of $0^\circ/90^\circ$ print orientation.

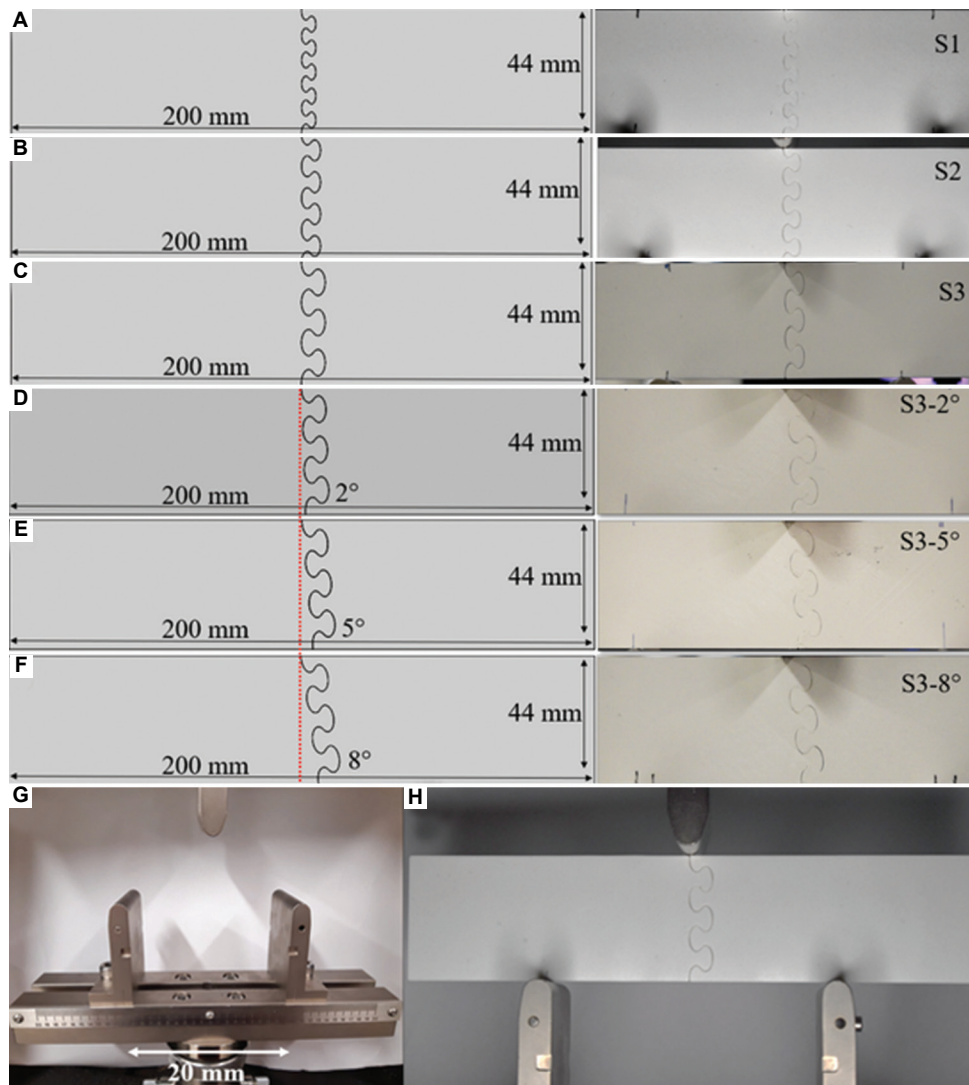


Figure 3. (A) S1 Schematic and PLA Specimen, (B) S2 Schematic and PLA Specimen, (C) S3 Schematic and PLA Specimen, (D) S3-2° Schematic and PLA Specimen, (E) S3-5° Schematic and PLA Specimen, (F) S3-8° Schematic and PLA Specimen, (G) three-point bending test setup, (H) three-point bending setup with specimen.

Table 1. Dimensions of the 3D printed PLA specimens

Specimen	Length (mm)	Width (mm)	Thickness (mm)	Minor radius, a (mm)	Major radius, b (mm)	Print layer height (mm)	Infill density	Number of print layers
S1	200	44	4	1.5	2.7	0.2	100%	20
S2	200	44	4	2	3.6	0.2	100%	20
S3	200	44	4	2.5	4.5	0.2	100%	20

Eq. 1 can be utilized to calculate the total circumference, C of the ellipse, while Eq. 2 and 3 can be utilized to calculate the arc length C' of the ellipse at a given angle. Minor radius – a , major radius – b , and the angle are shown in Figure 2A. Once the repeat length, as given in Figure 2A, is calculated, the total area can be obtained by multiplying the whole length by the thickness (T), which is 4 mm in all the specimens.

2.2. Flexural test

A three-point bending test was conducted according to ASTM D790 to analyze the behavior of the suture structures under flexural loading^[50]. A 5900R Instron universal testing machine with a 5 kN load cell and span length of 20 mm were utilized to perform the test. The length, height, and width of all the specimens were maintained to be 200 mm,

44 mm, and 4 mm, with a span length of 100 mm. The test setup without and with a PLA specimen is given in Figure 3G and H. The crosshead displacement rate was maintained to be 1 mm/min, and a 1 N preload was applied to ensure proper contact between the test specimen and the impactor. Five specimens were tested for each design. The centered cylindrical roller with 10 mm diameter and two supporting rollers at the bottom with 10 mm diameter were utilized to perform the three-point bending test.

2.3. DIC

DIC was conducted using Ncorr open source 2D Matlab software to analyze the strain field generation during the flexural test^[51]. The region of interest (ROI) for the DIC was carefully selected to obtain the maximum results. As the specimen was built by connecting two parts, during three-point bending, the two parts started to separate, and creating a gap between the parts; hence, to eliminate the negative impact on the DIC results, selecting the ROI was done separately for the two parts.

2.4. Numerical simulation

A finite element model to simulate the suture inspired structure under a three-point bending test was developed using ABAQUS/Explicit 2020 (Dassault Systems Simulia Corp., Providence, RI). Three rollers having 10 mm diameter were modeled, and the test specimen was placed between the rollers according to the actual experimental setup. Metal rollers are treated as rigid bodies for the simplification of the simulation since they are significantly rigid compared to the PLA specimens. The constitutive behavior of the suture inspired test specimens is considered to be elastic-perfectly plastic based on the literature^[52-55].

It is worth mentioning that the material anisotropy and localized defects that occur due to the 3D printing process are not considered in this analytical model. Through displacement boundary conditions, loading was applied to the top roller, while two bottom supporting rollers were encastered. Hard contact formulation was utilized to create normal contact behavior between the rollers and the test specimens, and tangential behavior was defined using penalty friction formulation with a friction coefficient of 0.3. A two-dimensional model was developed to save the cost and time of the simulation for S1, S2, S3, S3-2°, S3-5°, and S3-8° with 38029 linear quadrilateral elements of type CPS4R. The load of the top roller was further analyzed, and the bending stiffness of each specimen is calculated by the slope of the linear part of the force-displacement curve.

3. Results and discussion

3.1. Experimental results

The force-displacement curves of S1, S2, and S3 are given in Figure 4A. The number of suture ligaments in each design decreased with the increment of the size of the suture unit, thereby affecting the maximum load the structure can withstand before the failure. As per the force-displacement curves, it is evident that the S1 specimen withstand the highest load while the S2 specimen indicates the lowest maximum load. When it comes to the S3 specimen, the maximum load it can withstand had increased compared to S2 but was still lower than the S1. In all three cases, the force-displacement curves exhibit a similar pattern. Once the lowest suture ligament fails, the load suddenly drops, then starts to increase again and experiences another

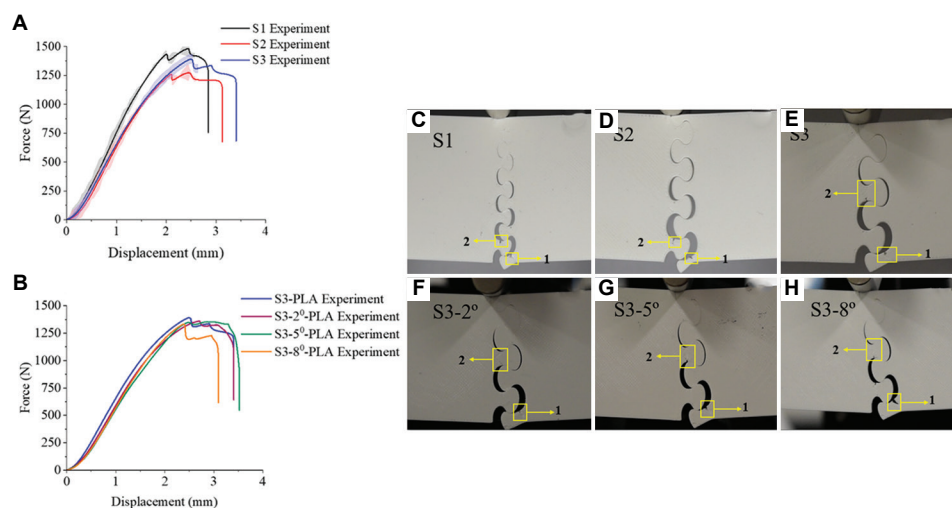


Figure 4. (A) Force-displacement curves of S1, S2, and S3. (B) Force-displacement curves of S3, S3-2°, S3-5°, and S3-8°; the failure points highlighted in yellow for (C) S1 - first & second points, (D) S2 - first & second points, (E) S3 - first & second points (F) S3-2°, (G) S3-5°, (H) S3-8°

sudden drop, it continues with a plateau until the failure of the whole structure.

As S3 exhibits the highest displacement, it implies that the S3 structure can absorb more energy by deforming than S1 and S2. Further studies on the effect of the positioning angle of the suture structure on flexural properties are conducted using the S3 specimen design. The positioning angles are varied by 2°, 5° and 8°. The positioning angles were varied by 2°, 5°, and 8° as given in Figure 3D-F. The maximum loads of S3-2°, S3-5°, and S3-8° designs were decreased, respectively, and all three maximum load values were lower than the maximum load of the S3 specimen. The total displacement of the S3-2° before the failure is almost similar to the S3, while S3-5° exhibits a larger displacement than S3. When it comes to S3-8°, the displacement significantly reduces compared to all the above-mentioned test specimens. The force-displacement curves are given in Figure 4B. These results indicate that the position of the suture components with respect to the applied load is a critical factor, and there is a possibility for further improvement of S3 by allocating the most suitable positioning angle.

In all the cases, failure first occurred at the semi suture module located at the bottom end of the suture component, indicated by first yellow square in Figure 4C-H. In all S3 samples, the second fracture point occurred in the middle of the suture module. In contrast, in S1 and S2, the second fracture point occurred closer to the first one, which implies in S3 specimens, stress is distributed evenly among all suture modules.

Flexural strength, bending stiffness, and energy absorbed by each design are given in Figure 5. As shown in Figure 5A, the flexural strength is significantly higher in the S1 sample than in S2 and S3. With the increment of the positioning angle, the flexural strength gradually decreases compared to the original S3 sample. The bending stiffness of each design is calculated using the force-displacement curve slope. Energy absorption is calculated using the area under the force-displacement curve. The bar charts indicate that bending stiffness decreases gradually with the increment of the positioning angle. Compared to S1, the absorbed energy of S2 and S3 is increased by 20% and 48%, respectively. Compared to S3, the energy absorption of S3-2°, S3-5°, and S3-8° is reduced by 4.2%, 1%, and 20%, respectively. Considering the flexural strength, bending stiffness, energy absorption, and failure pattern, different suture structures can be employed to achieve the desired performances. For example, the S1 design would perform better than S2 or S3, where higher flexural strength is required, and S3 would perform better than S1 or S2 in absorbing higher energy.

3.2. DIC results

DIC results of strain fields (ε) for S3, S3-2°, S3-5°, and S3-8° when the fracture starts to propagate are given in Figure 6A-D, respectively. Strains fields generated in both parts of the specimens are given in the images. The ROI was selected separately for the interlocked parts in the same specimen to obtain clear strain field contour plots. Higher strain along y-direction was visible in the weaker semi suture module at the bottom of the test specimen, which implies high-stress generation.

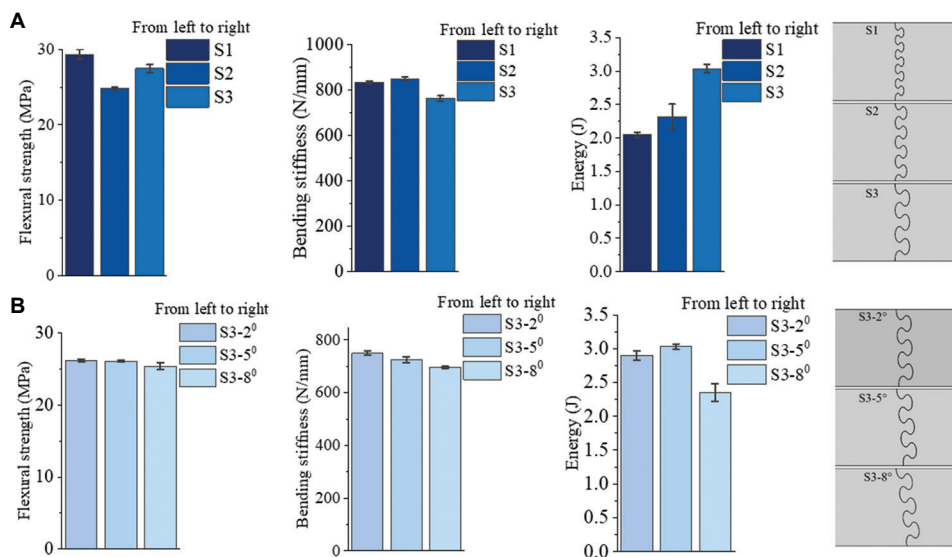


Figure 5. (A) Flexural strength, bending stiffness and energy absorption of S1, S2 and S3. (B) Flexural strength, bending stiffness and energy absorption of S3-2°, S3-5° and S3-8°.

From all DIC results, it is visible that one side of the necking area is under compression in every suture module while the other side of the necking area experiences tension. The force exerted by the top suture module causes tension on the necking area of the bottom suture module. Meanwhile, the top suture module gets compressed by the bottom suture module in return due to the interlocking feature. DIC contour plots of the S3 specimen show high-stress concentration in the suture modules, while with the increment of the inclined angle, stress is distributed more uniformly across all suture modules. This could be the reason for S3-2° and S3-5° specimens to have a slight increment in the displacement before the failure compared to the S3 one, as given in Figure 4B. In S3-2° and S3-5° specimens, stress is uniformly distributed among all the suture modules. Still, in the S3-8° specimen, stress is mainly concentrated at the weaker semi suture module at the bottom, causing failure at a lower displacement.

3.3. Comparison between experimental and numerical simulation results

The comparison between force-displacement curves obtained from numerical simulation and the experimental results for S1,

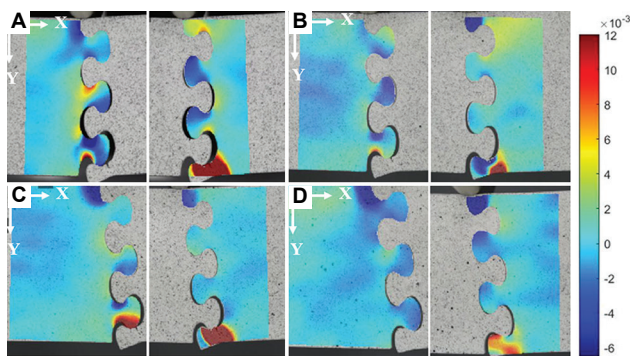


Figure 6. DIC contour plots of ϵ_{yy} strain fields for the two interlocked parts just before the fracture. (A) S3, (B) S3-2°, (C) S3-5°, and (D) S3-8°. Region of interest (ROI) is selected separately for the two parts of the same interlocked specimen.

S2, and S3 are shown in Figure 7A. The numerical simulation results show a good agreement with the experimental results with slight discrepancy due to the assumption of elastic-perfectly plastic material constitutive model. Figure 7B-D exhibits the deformation comparison of simulation and experimental results of S1, S2, and S3. Simulation results have captured the deformation of each suture design till the specimens reach their maximum loading conditions.

Compared to S1 and S2, sample S3 shows higher deformation, implying that the structure is more flexible. The number of interlocking points directly affects the structure’s flexibility and strength. Fewer interlocking points allow the structure to deform in a larger displacement, while many interlocking points make the structure stiffer. Force-displacement graphs from the experiment and simulation model for S3-2°, S3-5°, and S3-8° are given in Figure 8A. Numerical simulation results show good agreement with the experimental results up to the point of maximum load. Similar to the previous section, the slight difference between the experimental and simulation results is caused due to not considering the porosity effect of 3D printed structures and assuming the model behavior to be elastic perfectly plastic.

The deformation captured by the simulation and the experimental deformation for S3-2°, S3-5°, and S3-8° are shown in Figure 8B-D.

3.4. Parametric study

Many biological structures with sutures do not contain a single suture line throughout the whole structure, but rather a network of suture lines to create complex arrangements^[9,49,56]. Here, a simple parametric study was conducted to investigate the influence of two suture lines in the structure. For all three sizes, S1, S2, and S3 symmetrical suture lines with inclined angles of 0, 2, 5, and 8 degrees were incorporated in two different configurations as shown in Figure 9A and B. Specimens are created by connecting three separate parts to include two suture lines. The two

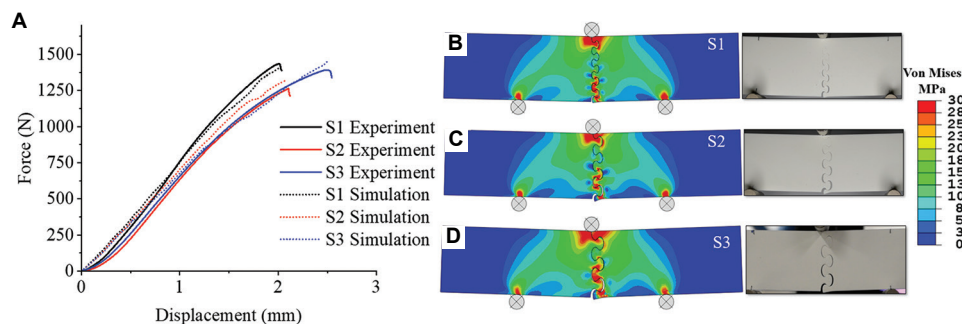


Figure 7. (A) Numerical simulation and experimental force-displacement results comparison of S1, S2 and S3. Von Mises stress distribution comparison at the maximum load of each design: (B) S1 simulation and experiment, (C) S2 simulation and experiment, and (D) S3 simulation and experiment.

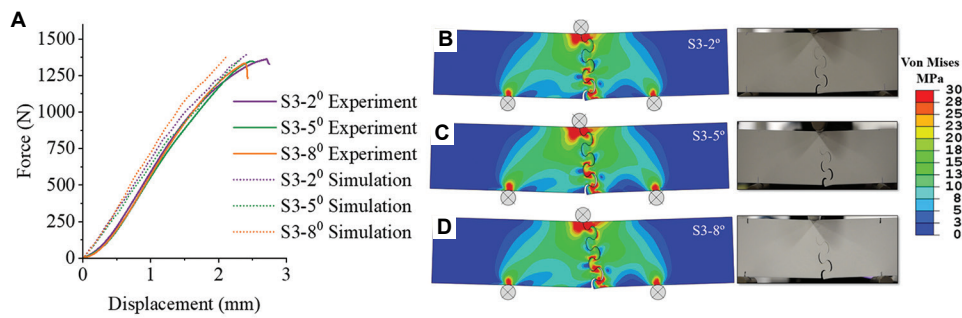


Figure 8. (A) Numerical simulation and experimental force-displacement results comparison of S3-2°, S3-5° and S3-8°. Von Mises stress distribution comparison at the maximum load of each design: (B) S3-2° simulation and experiment, (C) S3-5° simulation and experiment, and (D) S3-8° simulation and experiment.

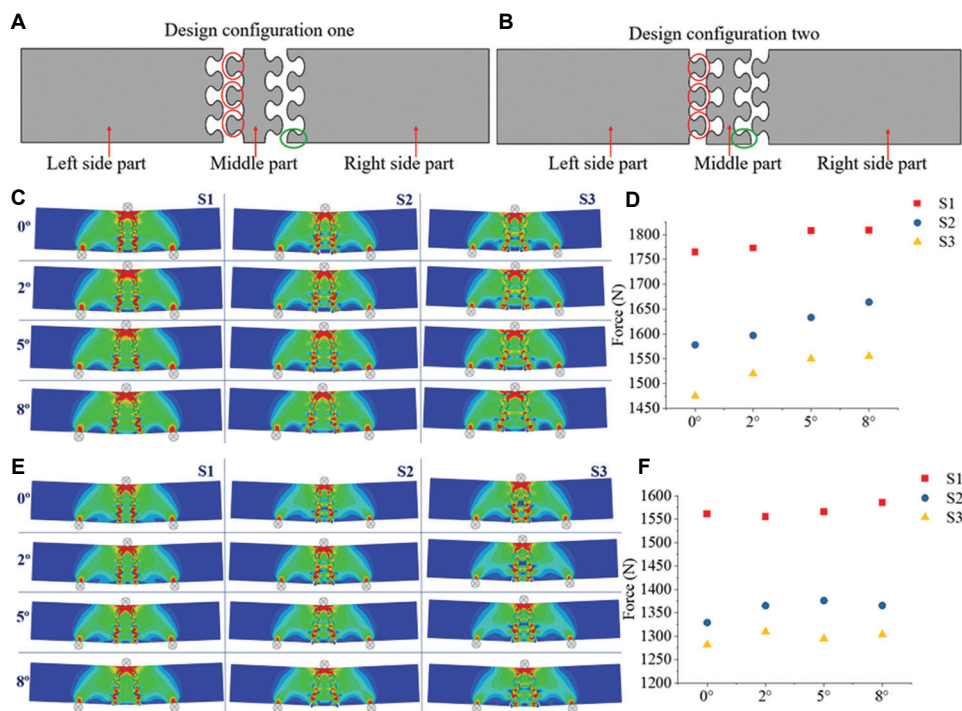


Figure 9. (A) Design configuration one, and (B) design configuration two; red circles indicate the placement of the interlocking suture modules on the side part and the middle part of the specimen, and green circle shows the weaker semi suture module. (C) Von Mises stress comparison of 0°, 2°, 5° and 8° inclined angle designs in configuration one. (D) Scatter plot of peak forces in each design. (E) Von Mises stress comparison of 0°, 2°, 5° and 8° inclined angle designs in configuration two. (F) Scatter plot of peak forces in each design.

design configurations are shown in Figure 9A and B. In configuration one, many numbers of interlocking suture modules were printed in the middle part of the specimen, and in configuration two, many interlocking suture modules were printed in the side parts of the specimen as highlighted in red circles. Figure 9C and E show the completed specimens of the two design configurations at their maximum load. Figure 9D and F show the scatter plots of the maximum force encountered by each design.

In all the cases, S1 yields the highest maximum force due to its many interlocking points compared to S2 and S3,

even though in all three cases, the areas covered by sutures are equal. Parametric results from design configuration one show that the maximum force gradually increases with the increment of the inclined angle. Despite small fluctuations in the maximum loads in design configuration two, the overall results present similar behavior to design configuration one. This implies that design configuration one could provide a more stable and predictable structure, as the force gradually increases with the increment of the angle without any fluctuations in the results, compared to configuration two.

Table 2 . The percentage increments of the maximum loads in design configuration one compared to the design configuration two

	S1	S2	S3
0°	13 %	18 %	15 %
2°	14 %	16 %	16 %
5°	15 %	18 %	19 %
8°	14 %	21 %	19 %

Comparing the results of design configurations one and two, as given in Figure 9A and B, the maximum load obtained by samples S1, S2, and S3 in configuration one is higher than in configuration two. The percentage increment of the maximum loads in design configuration one compared to the design configuration two is given in Table 2.

Similar to the experimental results, higher stress occurs in the bottom semi suture module in every design where the first failure occurs. In design configuration one, weaker bottom semi suture modules (highlighted in green circle in Figure 9A) are attached to the bigger side parts, where they gain support for the stress distribution; hence, this design configuration can withstand a higher load. In configuration two, weaker bottom semi suture modules (highlighted in green circle in Figure 9B) are connected to the middle part of the specimen, where it gains support only from the middle part for the stress distribution, as shown in Figure 9B. This leads the design configuration two to withstand a lower maximum load compared to the configuration one.

This parametric study showed that the maximum load the structure can withstand could be improved by combining symmetrical suture lines, correlating with the inclined angle increment. The placement of the weaker link within the suture structure also significantly impacts the highest load the structure can withstand.

4. Conclusion

The research was conducted to investigate the flexural behavior of bio-inspired suture structures. The specimens were developed with three different sizes as S1, S2, and S3 using 3D printing of PLA thermoplastic while maintaining the ratio between the minor and major radii of the elliptical suture shape to 1:1.8. S3 design was used to develop S3-2°, S3-5°, and S3-8°, varying the positioning angles by 2°, 5°, and 8° to analyze the effect of the positioning angle. The S1 specimen withstood maximum load during the three-point bending test but failed within short displacement, whereas S3 showed higher displacement before the failure but with a lower maximum load. The flexural strengths of S1, S2, and S3 were noted to be 28 MPa, 24 MPa, and 26 MPa, while the energy absorption of each design was calculated

as 2 J, 2.5 J, and 3 J. Bending stiffness values indicate that compared to S1, both S2 and S3 designs are harder to bend.

- (i) When changing the positioning angle of the suture component, the total displacement before the failure was slightly increased compared to the S3, in both S3-2° and S3-5°. Further increment in the angle up to 8° has noticeably reduced the total displacement at failure compared to S3 specimen as the stress is concentrated mainly in the weaker semi suture module at the bottom rather than uniformly distributing through the whole suture structure. In all three cases, flexural strengths and energy absorptions were slightly reduced compared to S3. The variation in bending stiffness values suggests that by changing the positioning angle of the sutures, the stiffness of the whole structure could be improved.
- (ii) DIC results indicate that adjacent interlocking suture modules exert tension and compression on each other due to their interlocking feature. When the top suture modules exert tension on the necking area of the bottom suture module, the head of the bottom suture module curls up and compresses the top suture module, and instead of moving down before fracture occurs in its necking area.
- (iii) Numerical simulation showed good agreement with the experimental results. The model was assumed to be elastic-perfectly plastic, even though FDM prints contain defects due to the printing process. The model reveals that introducing larger suture modules with less interlocking points allows more uniform stress distribution along the suture structure compared to S1 and S2, where the stress was mainly concentrated to the suture modules at the bottom of the specimen.
- (iv) The parametric study was performed on beam samples with two symmetrical suture lines, which considerably enhanced the ability to withstand a higher load. The load-bearing ability of the structure was further improved with the increment of the inclined angle. The simulation results also confirm that positioning of the interlocking suture modules plays an important role in enhancing the load-bearing properties of the structure. The parametric study concluded that the position of the suture components has a significant impact on the mechanical performance of the whole structure.
- (v) These sutures could be beneficial in many ways when developing a structural design. Incorporating a suture joint creates a pre-established crack path which would help to predict the fracture behavior by analyzing the suture pattern while maintaining flexibility. As the suture joint is developed without any adhesive materials, this interlocking mechanism

could be utilized to join dissimilar materials without any external joining treatments. Finally, large modular parts could be manufactured by connecting small pieces through the interlocking technique without limiting to the small part volume in many 3D printers.

Based on our results, we conclude that depending on the desired mechanical performance, different suture designs can be utilized to achieve a decent outcome. For example, when high energy absorption is required, S3 design could be benefited, and when a higher load-bearing action is required, S1 design could be highly effective. From the results of this research, it is evident that bio-inspired suture structures can be further optimized to enhance their performances, providing countless advantages for many engineering applications.

Acknowledgments

The authors acknowledge the facilities and the scientific and technical assistance of the Advanced Manufacturing Precinct, the Rheology and Materials Characterization Laboratory at RMIT University.

Funding

This research received no external funding.

Conflict of interest

The authors declare no conflict of interest.

Author contributions

Conceptualization: Phuong Tran

Data curation: Sachini Wickramasinghe

Funding acquisition: Truong Do

Methodology: Phuong Tran

Supervision: Phuong Tran

Writing—original draft: Sachini Wickramasinghe

Writing—review and editing: Truong Do, Phuong Tran

All authors have read and agreed to the published version of the manuscript.

References

- Ghazlan A, Ngo T, Tan P, *et al.*, 2021, Inspiration from nature's body armours—a review of biological and bioinspired composites. *Compos B Eng*, 205: 108513.
<https://doi.org/10.1016/j.compositesb.2020.108513>
- Ahamed MK, Wang H, Hazell PJ, 2022, From biology to biomimicry: Using nature to build better structures a review. *Constr Build Mater*, 320: 126195.
<https://doi.org/10.1016/j.conbuildmat.2021.126195>
- Du Plessis A, Broeckhoven C, Yadroitsava I, *et al.*, 2019, Beautiful and functional: A review of biomimetic design in additive manufacturing. *Addit Manuf*, 27: 408–427.
<https://doi.org/10.1016/j.addma.2019.03.033>
- Plocher J, Mencattelli L, Narducci F, *et al.*, 2021, Learning from nature: Bio-inspiration for damage-tolerant high-performance fibre-reinforced composites. *Compos Sci Technol*, 208: 108669.
<https://doi.org/10.1016/j.compscitech.2021.108669>
- Liu J, Li S, Fox K, *et al.*, 2022, 3D concrete printing of bioinspired bouligand structure: A study on impact resistance. *Addit Manuf*, 50: 102544.
<https://doi.org/10.1016/j.addma.2021.102544>
- Tee YL, Maconachie T, Pille P, *et al.*, 2021, From nature to additive manufacturing: Biomimicry of porcupine quill. *Mater Des*, 210: 110041.
<https://doi.org/10.1016/j.matdes.2021.110041>
- Peng C, Tran P, 2020, Bioinspired functionally graded gyroid sandwich panel subjected to impulsive loadings. *Compos B Eng*, 188: 107773.
<https://doi.org/10.1016/j.compositesb.2020.107773>
- Achrai B, Wagner HD, 2013, Micro-structure and mechanical properties of the turtle carapace as a biological composite shield. *Acta Biomater*, 9: 5890–5902.
<https://doi.org/10.1016/j.actbio.2012.12.023>
- Krauss S, Monsonogo-Ornan E, Zelzer E, *et al.*, 2009, Mechanical function of a complex three-dimensional suture joining the bony elements in the shell of the red-eared slider turtle. *Adv Mater*, 21: 407–412.
<https://doi.org/10.1002/adma.200801256>
- Lee N, Horstemeyer M, Rhee H, *et al.*, 2014, Hierarchical multiscale structure-property relationships of the red-bellied woodpecker (*Melanerpes carolinus*) beak. *J R Soc Interf*, 11: 20140274.
<https://doi.org/10.1098/rsif.2014.0274>
- Liu Z, Zhang Z, Ritchie RO, 2020, Interfacial toughening effect of suture structures. *Acta Biomater*, 102: 75–82.
<https://doi.org/10.1016/j.actbio.2019.11.034>
- Vincent JF, Wegst UG, 2004, Design and mechanical properties of insect cuticle. *Arthrop Struct Dev*, 33: 187–99.
<https://doi.org/10.1016/j.asd.2004.05.006>
- Yang W, Naleway SE, Porter MM, *et al.*, 2015, The armored carapace of the boxfish. *Acta Biomater*, 23: 1–10.
<https://doi.org/10.1016/j.actbio.2015.05.024>
- Magwene PM, Socha JJ, 2013, Biomechanics of turtle shells: How whole shells fail in compression. *J Exp Zool A Ecol*

- Genet*, 319: 86–98.
<https://doi.org/10.1002/jez.1773>
15. Jia Z, Yu Y, Wang L, 2019, Learning from nature: Use material architecture to break the performance tradeoffs. *Mater Des*, 168: 107650.
<https://doi.org/10.1016/j.matdes.2019.107650>
 16. Chen IH, Yang W, Meyers MA, 2015, Leatherback sea turtle shell: A tough and flexible biological design. *Acta Biomater*, 28: 2–12.
<https://doi.org/10.1016/j.actbio.2015.09.023>
 17. Alheit B, Bargmann S, Reddy B, 2020, Computationally modelling the mechanical behaviour of turtle shell sutures a natural interlocking structure. *J Mech Behav Biomed Mater*, 110: 103973.
<https://doi.org/10.1016/j.jmbbm.2020.103973>
 18. Gao C, Li Y, 2019, Mechanical model of bio-inspired composites with sutural tessellation. *J Mech Phys Solids*, 122: 190–204.
<https://doi.org/10.1016/j.jmps.2018.09.015>
 19. Lin E, Li Y, Ortiz C, *et al.*, 2014, 3D printed, bio-inspired prototypes and analytical models for structured suture interfaces with geometrically-tuned deformation and failure behavior. *J Mech Phys Solids*, 73: 166–182.
<https://doi.org/10.1016/j.jmps.2014.08.011>
 20. Malik IA, Mirkhalaf M, Barthelat F, 2017, Bio-inspired “jigsaw”-like interlocking sutures: Modeling, optimization, 3D printing and testing. *J Mech Phys Solids*, 102: 224–238.
<https://doi.org/10.1016/j.jmps.2017.03.003>
 21. Schmidt MJ, Farke D, Staszuk C, *et al.*, 2022, Closure times of neurocranial sutures and synchondroses in Persian compared to Domestic Shorthair cats. *Sci Rep*, 12: 1–13.
<https://doi.org/10.1038/s41598-022-04783-1>
 22. Nicolay CW, Vaders MJ, 2006, Cranial suture complexity in white-tailed deer (*Odocoileus virginianus*). *J Morphol*, 267: 841–849.
<https://doi.org/10.1002/jmor.10445>
 23. Bailleul AM, Scannella JB, Horner JR, *et al.*, 2016, Fusion patterns in the skulls of modern archosaurs reveal that sutures are ambiguous maturity indicators for the Dinosauria. *PLoS One*, 11: e0147687.
<https://doi.org/10.1371/journal.pone.0147687>
 24. Rivera J, Hosseini MS, Restrepo D, *et al.*, 2020, Toughening mechanisms of the elytra of the diabolical ironclad beetle. *Nature*, 586: 543–548.
 25. Arakane Y, Lomakin J, Gehrke SH, *et al.*, 2012, Formation of rigid, non-flight forewings (elytra) of a beetle requires two major cuticular proteins. *PLoS Genet*, 8: e1002682.
<https://doi.org/10.1371/journal.pgen.1002682>
 26. Fédrigo O, Wray GA, 2010, Developmental evolution: How beetles evolved their shields. *Curr Biol*, 20: R64–R66.
<https://doi.org/10.1016/j.cub.2009.12.012>
 27. Linz DM, Hu AW, Sitvarin MI, *et al.*, 2016, Functional value of elytra under various stresses in the red flour beetle, *Tribolium castaneum*. *Sci Rep*, 6: 1–10.
<https://doi.org/10.1038/srep34813>
 28. Tomoyasu Y, Arakane Y, Kramer KJ, *et al.*, 2009, Repeated co-options of exoskeleton formation during wing-to-elytron evolution in beetles. *Curr Biol*, 19: 2057–2065.
<https://doi.org/10.1016/j.cub.2009.11.014>
 29. Chen PY, 2020, Diabolical ironclad beetles inspire tougher joints for engineering applications. *Nature*, 586: 502–504.
<https://doi.org/10.1038/d41586-020-02840-1>
 30. Lazarus BS, Velasco-Hogan A, Gómez-del Río T, *et al.*, 2020, A review of impact resistant biological and bioinspired materials and structures. *J Mater Res Technol*, 9: 15705–15738.
<https://doi.org/10.1016/j.jmrt.2020.10.062>
 31. Huang W, Restrepo D, Jung JY, *et al.*, 2019, Multiscale toughening mechanisms in biological materials and bioinspired designs. *Adv Mater*, 31: 1901561.
<https://doi.org/10.1002/adma.201901561>
 32. Studart AR, 2016, Additive manufacturing of biologically-inspired materials. *Chem Soc Rev*, 45: 359–376.
<https://doi.org/10.1039/C5CS00836K>
 33. Gharde S, Surendren A, Korde JM, *et al.*, 2019, Recent advances in additive manufacturing of bio-inspired materials. In: *Biomufacturing*, Springer, Berlin, p35–68.
https://doi.org/10.1007/978-3-030-13951-3_2
 34. Dev S, Srivastava R, 2021, Effect of infill parameters on material sustainability and mechanical properties in fused deposition modelling process: A case study. *Prog Addit Manuf*, 6: 631–642.
 35. Gu GX, Chen CT, Richmond DJ, *et al.*, 2018, Bioinspired hierarchical composite design using machine learning: simulation, additive manufacturing, and experiment. *Mater Horiz*, 5: 939–945.
<https://doi.org/10.1039/C8MH00653A>
 36. Dimas LS, Buehler M, 2014, Modeling and additive manufacturing of bio-inspired composites with tunable fracture mechanical properties. *Soft Matter*, 10: 4436–4442.
<https://doi.org/10.1039/C3SM52890A>
 37. Samykano M, Selvamani S, Kadirgama K, *et al.*, 2019, Mechanical property of FDM printed ABS: Influence of printing parameters. *Int J Adv Manuf Technol*, 102: 2779–

2796.
<https://doi.org/10.1007/s00170-019-03313-0>
38. Mazzanti V, Malagutti L, Mollica F, 2019, FDM 3D printing of polymers containing natural fillers: A review of their mechanical properties. *Polymers*, 11: 1094.
<https://doi.org/10.3390/polym11071094>
39. Cuiffo MA, Snyder J, Elliott AM, *et al.*, 2017, Impact of the fused deposition (FDM) printing process on polylactic acid (PLA) chemistry and structure. *Appl Sci*, 7: 579.
<https://doi.org/10.3390/app7060579>
40. Luis E, Pan HM, Sing SL, *et al.*, 2020, 3D direct printing of silicone meniscus implant using a novel heat-cured extrusion-based printer. *Polymers*, 12: 1031.
<https://doi.org/10.3390/polym12051031>
41. Velasco-Hogan A, Xu J, Meyers MA, 2018, Additive manufacturing as a method to design and optimize bioinspired structures. *Adv Mater*, 30: 1800940.
<https://doi.org/10.1002/adma.201800940>
42. Wang D, Chen D, Chen Z, 2020, Recent progress in 3D printing of bioinspired structures. *Front Mater*, 7: 286.
<https://doi.org/10.3389/fmats.2020.00286>
43. Ehrmann G, Ehrmann A, 2021, Investigation of the shape-memory properties of 3D printed PLA structures with different infills. *Polymers*, 13: 164.
<https://doi.org/10.3390/polym13010164>
44. Raj SA, Muthukumaran E, Jayakrishna K, 2018, A case study of 3D printed PLA and its mechanical properties. *Mater Today Proc*, 5: 11219–26.
<https://doi.org/10.1016/j.matpr.2018.01.146>
45. Kiendl J, Gao C, 2020, Controlling toughness and strength of FDM 3D-printed PLA components through the raster layup. *Compos B Eng*, 180: 107562.
<https://doi.org/10.1016/j.compositesb.2019.107562>
46. Rajpurohit SR, Dave HK, 2018, Effect of process parameters on tensile strength of FDM printed PLA part. *Rapid Prototyp J*, 24: 1317–1324.
<https://doi.org/10.1108/RPJ-06-2017-0134>
47. Cao Y, Wang W, Wang J, *et al.*, 2019, Experimental and numerical study on tensile failure behavior of bionic suture joints. *J Mech Behav Biomed Mater*, 92: 40–49.
<https://doi.org/10.1016/j.jmbbm.2019.01.001>
48. Malik IA, Barthelat F, 2018, Bioinspired sutured materials for strength and toughness: Pullout mechanisms and geometric enrichments. *Int J Solids Struct*, 138: 118–133.
<https://doi.org/10.1016/j.ijsolstr.2018.01.004>
49. Miura T, Perlyn CA, Kinboshi M, *et al.*, 2009, Mechanism of skull suture maintenance and interdigitation. *J Anat*, 215: 642–655.
<https://doi.org/10.1111/j.1469-7580.2009.01148.x>
50. Standard A, 2014, ASTM D638-14 Standard Test Method for Tensile Properties of Plastics. ASTM International, West Conshohocken, PA.
51. Blaber BA, Antoniou A, 2015, Ncorr: Open-source 2D digital image correlation matlab software. *Exp Mech*, 55: 1105–1122.
52. Peng C, Fox K, Qian M, *et al.*, 2021, 3D printed sandwich beams with bioinspired cores: Mechanical performance and modelling. *Thin Walled Struct*, 161: 107471.
<https://doi.org/10.1016/j.tws.2021.107471>
53. Habib F, Iovenitti P, Masood S, *et al.*, 2017, In-plane energy absorption evaluation of 3D printed polymeric honeycombs. *Virtual Phys Prototyp*, 12: 117–131.
<https://doi.org/10.1080/17452759.2017.1291354>
54. Kardel K, Ghaednia H, Carrano AL, *et al.*, Experimental and theoretical modeling of behavior of 3D-printed polymers under collision with a rigid rod. *Addit Manuf*, 14: 87–94.
<https://doi.org/10.1016/j.addma.2017.01.004>
55. Lee SH, Lee KG, Hwang JH, *et al.*, 2019, Evaluation of mechanical strength and bone regeneration ability of 3D printed kagome-structure scaffold using rabbit calvarial defect model. *Mater Sci Eng C*, 98: 949–959.
<https://doi.org/10.1016/j.msec.2019.01.050>
56. Liu L, Jiang Y, Boyce M, *et al.*, 2017, The effects of morphological irregularity on the mechanical behavior of interdigitated biological sutures under tension. *J Biomech*, 58: 71–78.
<https://doi.org/10.1016/j.jbiomech.2017.04.017>